

Modeling snow-crystal growth: A three-dimensional mesoscopic approach

Janko Gravner*

Mathematics Department, University of California, Davis, California 95616, USA

David Griffeath†

Department of Mathematics, University of Wisconsin, Madison, Wisconsin 53706, USA

(Received 11 April 2008; revised manuscript received 30 October 2008; published 6 January 2009)

We introduce a three-dimensional, computationally feasible, mesoscopic model for snow-crystal growth, based on diffusion of vapor, anisotropic attachment, and a boundary layer. Several case studies are presented that faithfully replicate most observed snow-crystal morphology, an unusual achievement for a mathematical model. In particular, many of the most striking physical specimens feature both facets and branches, and our model provides an explanation for this phenomenon. We also duplicate many other observed traits, including ridges, ribs, sandwich plates, and hollow columns, as well as various dynamic instabilities. The concordance of observed phenomena suggests that the ingredients in our model are the most important ones in the development of physical snow crystals.

DOI: [10.1103/PhysRevE.79.011601](https://doi.org/10.1103/PhysRevE.79.011601)

PACS number(s): 81.10.Aj, 61.50.Ah

I. INTRODUCTION

In this paper we exhibit some *virtual snowflakes* generated by a natural, fully three-dimensional algorithm for snow-crystal evolution. The present study extends our earlier work on growth and deposition [1–3], and other previous efforts in this direction [4,5]. The key features of our model are *diffusion* of vapor, *anisotropic attachment* of water molecules, and a narrow *boundary layer*. All three ingredients seem to be essential for faithful emulation of the morphology observed in nature.

Growth of a snow crystal in a homogeneous environment, that is, in constant weather conditions, is primarily dependent on temperature, pressure, and vapor density. However, the principles by which these determine how supersaturated vapor attaches to a growing ice crystal are poorly understood [6]. Therefore, incorporating this process into a mathematical model in terms of tunable parameters is a sensible strategy. While it is not *a priori* clear how our parameters correlate with physical conditions, experimentation provides valuable clues (see Sec. VII–XIII). This approach also makes it possible to model inhomogeneous environments by varying the parameters during the evolution (see Sec. XII). As a reasonable first step, the diffusion of latent heat, generated by solidification [6], is neglected, as are surface diffusion [6], impedance [7], and other effects that may be important in some regimes. Based on the verisimilitude of virtual snowflakes in comparison to actual snow crystals (the most convenient resource for such comparison is Libbrecht’s field guide [8]), it would appear that this approach is able to shed light on a substantial portion of snow-crystal physics.

Our algorithm assumes a mesoscopic (micrometer) scale of basic units for the ice crystal and water vapor, which eliminates inherent randomness in the diffusion and the attachment mechanism. This brings the process within reach of realistic simulation; by contrast, any three-dimensional ap-

proach based on microscopic dynamics is completely beyond the scope of present computing technology. Moreover, there is ample evidence in the literature that the mesoscopic scale is more than a matter of expedience. In snow crystals, the surface defects known as *microsteps* that induce layer-by-layer faceted growth often tend to bunch, creating micrometer-scale *macrostep* dislocations [9,10]. Recent photomicrographs (e.g., [11]) provide convincing corroboration for these structural features. We suspect that macrostep processes promote a separation of scales that underlies the success of our approach. We refer the reader to [3] for a brief history of snow-crystal observation and modeling, the background for a two-dimensional version of our algorithm, and many references to the literature. See also [12] for another attempt at spatial mesoscopic modeling.

There are many papers and books, for a variety of audiences, dealing with snowflake photography and classification, the underlying physics, or some combination thereof, so we will not offer a comprehensive review here. Excellent introductions to the subject include the classic book by Nakaya [13], early empirical studies and classification schemes [14,15], and more recent papers and books by Libbrecht [16–18,6,19,20]. Among research papers that attempt to decipher the three-dimensional aspects of snow crystals, the standout reference is [21]; also worth mentioning are [22–25].

As a preview of the capabilities of our model, let us illustrate the crystal tip instability and initiation of side branching studied in the laboratory by Gonda and Nakahara [11]. A sequence of four still frames from their paper was reproduced in [3] so we will not show it here. But Fig. 1 depicts the top view of a corresponding virtual snowflake at four different times (12 000, 15 000, 18 000, and 21 000), and oblique views of the crystal’s top and bottom at the final time. The parameters are $\beta_{01}=2.8$, $\beta_{10}=\beta_{20}=2.2$, $\beta_{11}=\beta_{21}=1.6$, $\beta_{30}=\beta_{31}=1$, $\kappa=0.005$, $\mu_{10}=\mu_{20}=0.001$, $\mu=0.0001$ otherwise, $\phi=0.01$, and $\rho=0.12$. Their role, and that of the initial state, will be described in Sec. II. The similarity between the real and simulated sequences is striking: in both instances a defect arises at a characteristic distance from the

*gravner@math.ucdavis.edu

†griffeat@math.wisc.edu

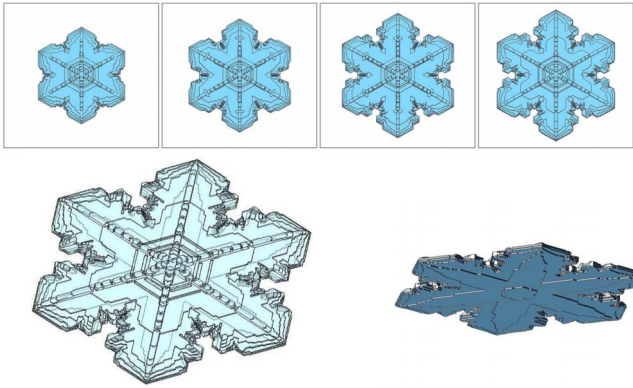


FIG. 1. (Color online) Tip instability and oblique top (left) and bottom (right) views of the final crystal.

crystal tip, becomes more pronounced, and later gives rise to a sidebranch with its own ridge structure similar to that of the main branch. Note also that our virtual snowflake has its ridges, and most other markings, on the top side; the bottom is almost featureless. This is due to a small downward drift in our model, an aspect we will discuss later in more detail. The direction of the drift represents the motion of the crystal in the opposite direction—we prefer upward motion because interesting features then appear on top, although this would obviously correspond to the bottom of a falling snowflake. We should also note that the drift value means that, during its evolution, our simulated crystal moved for about 200 space units, which is comparable to the diameter it reached. This is typical of drift values that erase features on one side without otherwise significantly changing the morphology. Our model thus predicts that, during growth, a significantly larger range of motion relative to the surrounding vapor is not possible for most interesting physical snow crystals such as dendrites or plates.

Another example of our algorithm’s potential to make predictions about basic aspects of snow-crystal growth is the location of markings. From micrographs, it is almost impossible to tell whether these are on the top or bottom of or inside a given physical specimen, so little attention has been paid to this issue to date. We have gathered a considerable amount of evidence that interior markings are quite common (see Secs. VII–IX).

Our account will focus on seven case studies that reproduce many features commonly observed in actual snowflakes: ridges, ribs, flumes and other “hieroglyphs,” formation of sidebranches, emergence of sandwich plates, hollow columns, hollow prism facets, and so forth. We also explore dependence on the density of vapor, the aforementioned effect of drift, and inhibition of sidebranches by the boundary layer. Varying meteorological conditions during growth are considered very important [8] so we include several examples, such as plates with dendritic tips and capped columns that are believed to arise due to sudden changes in the weather. However, we will encounter virtual snowflakes that grew in a homogeneous environment but give the impression they did not. We will occasionally address dependence of the final crystal on its early development, and conclude with a few eccentric examples that may be too brittle to occur in

nature. These typically arise near a phase boundary, when the dominant direction of growth is precarious. A complete collection of virtual snowflakes from our case studies (with some additional information, such as simulation array sizes), a collection of movies, and a slide show are available for download [36].

The first order of business, in the next section, is to describe the virtual snowflake algorithm in detail. Four subsequent sections discuss computer implementation and visualization tools, mathematical foundations, parameter tuning, and extensions of the model. The remainder of the paper is then devoted to the case studies.

II. THE ALGORITHM FOR THREE-DIMENSIONAL SNOW-CRYSTAL GROWTH

Our basic assumptions are as follows.

(A1) The mesoscopic (micrometer-scale) building blocks are (appropriately scaled) translates of the *fundamental prism*, which has a hexagonal base of side length $1/\sqrt{3}$ and height 1.

(A2) In its early stages of growth, from microscopic to mesoscopic, the crystal forms a hexagonal prism, and then it maintains this shape until it reaches the size of a few micrometers across.

(A3) Diffusion outside the crystal is isotropic except possibly for a small drift in the vertical direction.

(A4) Crystallization rates depend on the direction and local convexity at the boundary.

(A5) Melting at the crystal edge creates a boundary layer.

The side (rectangular) faces of the fundamental prism are commonly referred to as *prism* faces, while the top and bottom (hexagonal) ones are called *basal* faces.

The lattice for our model is $\mathbb{T} \times \mathbb{Z}$, where \mathbb{T} is the planar triangular lattice (see Fig. 2). This is not precisely the crystalline lattice of hexagonal ice Ih , which is obtained by removing certain edges and sites from $\mathbb{T} \times \mathbb{Z}$, and then applying a periodic deformation [12], but we are constructing a mesoscopic model that should obscure such fine details. Therefore, each $x \in \mathbb{T} \times \mathbb{Z}$ has eight neighbors: six in the \mathbb{T} direction and two in the \mathbb{Z} direction.

At each discrete time $t=0, 1, 2, \dots$, $A_t \subset \mathbb{T} \times \mathbb{Z}$ represents the virtual snowflake, and with each site $x \in \mathbb{T} \times \mathbb{Z}$ we associate two varieties of mass:

$b_t(x)$ = the *boundary mass* at x at time t

(frozen if $a_t(x) = 1$, unfrozen if $a_t(x) = 0$),

$d_t(x)$ = the *diffusive mass* at x at time t

(vapor).

The state of the system at time t at site x is therefore $(a_t(x), b_t(x), d_t(x))$, where a_t is the attachment flag,

$$a_t(x) = \begin{cases} 1 & \text{if } x \in A_t, \\ 0 & \text{otherwise.} \end{cases}$$

Our dynamics assumes that the diffusive and the unfrozen mass both change to ice when the site joins the crystal, and

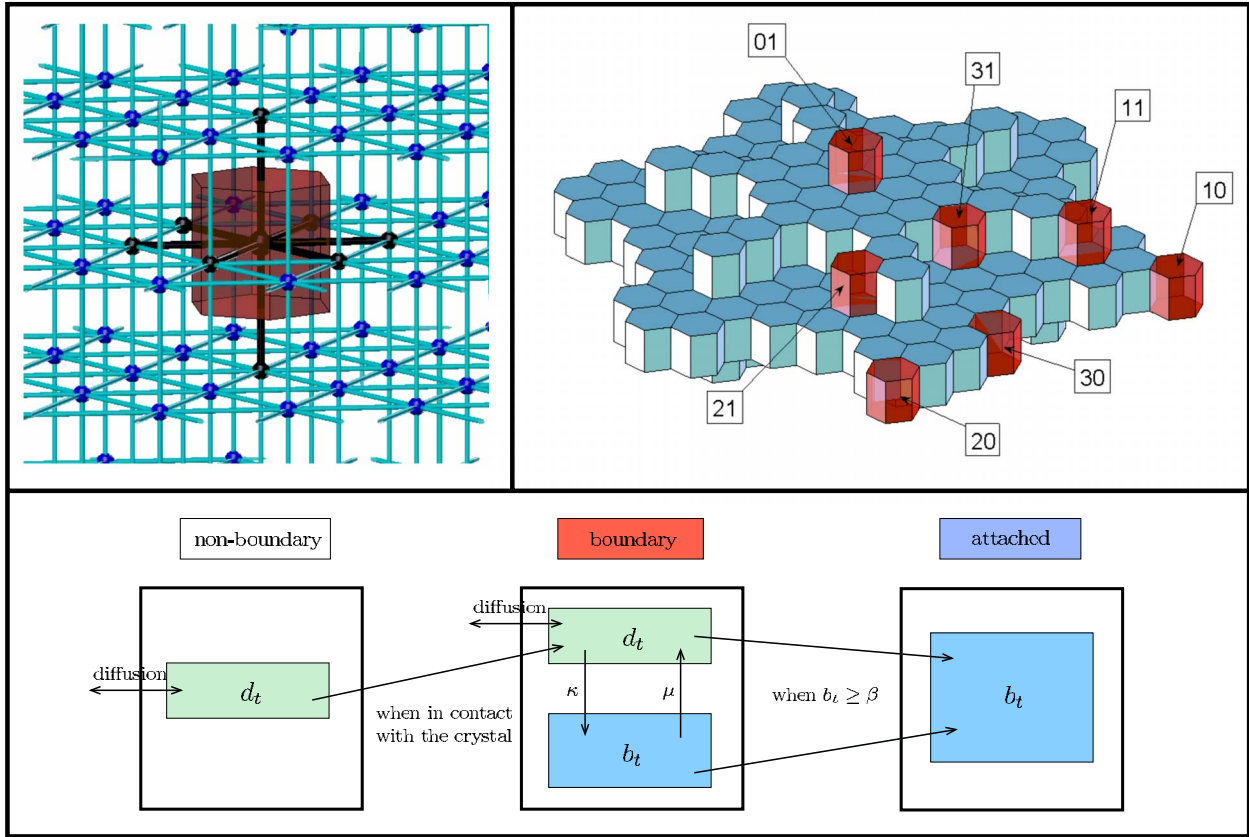


FIG. 2. (Color online) At the upper left is a portion of the underlying stacked triangular lattice $\mathbb{T} \times \mathbb{Z}$. The central site represented as a larger black ball has its neighborhood indicated in black, and a translate of the fundamental prism is centered at that site. In the upper right detail, translates of the fundamental prism are drawn around each site of a small crystal. Seven boundary sites are also depicted and each is labeled by two counts determined by its boundary configuration. For example, the “21” site has 2 horizontal (\mathbb{T}) neighbors and 1 vertical (\mathbb{Z}) neighbor; consequently, this site needs boundary mass β_{21} to join the crystal. The lower panel shows a flowchart for the algorithm. There are three epochs in the life of a site. Away from the crystal’s boundary, it only exchanges diffusive mass d_t with its neighbors. Once the crystal grows to reach the site’s neighborhood, two additional effects, melting and freezing, promote exchange between diffusive mass d_t and boundary mass b_t . Final changes occur once the boundary mass exceeds the threshold β (which depends on the boundary configuration): the site attaches and the two types of mass merge into b_t .

stay in that state thereafter. The two types of mass can coexist on the boundary of the virtual snowflake, but only boundary mass persists inside the virtual snowflake, while only diffusive mass occurs outside and away from the boundary. A conceptual summary of the dynamics is provided by Fig. 2. We encourage the reader to consult it often as a supplement to the dry mathematical description that follows.

It should be noted that there are only two mass fields, one of which (d_t) diffuses while the other (b_t) is stationary. The boundary layer dynamics, whereby a portion of the boundary mass b_t can change back to d_t , is a crude attempt to capture something of the hybrid state of a snow crystal’s *quasiliquid layer* [26], while keeping our algorithm as simple as possible. It is perhaps surprising that, despite this gross oversimplification, which ignores key features such as surface mobility, our model reproduces growth processes as well as it does. It is also important to note that close to the bulk melting point, where the (anisotropic) thickness of the physical quasiliquid layer diverges, our model is much less realistic than at lower temperatures.

The initial state will consist of frozen mass 1 at each site of some finite set, on which also $a_0 \equiv 1$, with a_0 and $b_0 \equiv 0$

and $d_0 \equiv \rho$ everywhere else. In keeping with assumption A2, the most natural choice for this finite set, a singleton at the origin, often does not work well, as its \mathbb{Z} -direction neighbors see seven neighbors off the crystal’s boundary. This means that it is common, even for low ρ , that the dynamics immediately triggers a rapid expansion in the \mathbb{Z} direction. To prevent this singularity, our canonical initial state consists of a hexagon of radius 2 and thickness 1, consisting of 20 sites. Other nonsymmetric initial states will be discussed later.

Let us now describe the update rule of our snowflake simulator, which performs steps (1)–(4) below in order every discrete time unit. The reader should observe that total mass is conserved by each step, and hence by the dynamics as a whole.

The set

$$\mathcal{N}_x^{\mathbb{T}} = \{x\} \cup \{y: y \text{ is a neighbor of } x \text{ in the } \mathbb{T} \text{ direction}\}$$

is called the \mathbb{T} neighborhood of x and consists of x together with its six neighbors in the direction of the triangular lattice \mathbb{T} , visualized as horizontal in Fig. 2. Similarly, the set $\mathcal{N}_x^{\mathbb{Z}} = \{x\} \cup \{y: y \text{ is a neighbor of } x \text{ in the } \mathbb{Z} \text{ direction}\}$ is the \mathbb{Z}

neighborhood of x and consists of x together with its two neighbors in the direction of the vertical \mathbb{Z} direction. We let $\mathcal{N}_x = \mathcal{N}_x^T \cup \mathcal{N}_x^Z$ be the set comprising x and all its eight neighbors. The (outside) boundary of the virtual snowflake at time t is then $\partial A_t = \{x \notin A_t : y \in A_t \text{ for some } y \in \mathcal{N}_x\}$ and we let $\bar{A}_t = A_t \cup \partial A_t$.

The complement of a set A is denoted by A^c . Also, we use degree and prime notation to denote the amounts of mass before and after a step or substep is completed. If there is more than one intermediate step, we use double primes. This is necessary since some mass allocations may change more than once during a single cycle of the steps. At the end of each cycle the time t advances to $t+1$.

A. Steps of the update rule

1. Diffusion

Diffusive mass evolves on A_t^c in two, or possibly three, substeps. The first substep is by discrete diffusion with uniform weight $\frac{1}{7}$ on the center site and each of its \mathbb{T} neighbors. Reflecting boundary conditions are used at the edge of the crystal. In other words, for $x \in \bar{A}_t^c$,

$$d'_t(x) = \frac{1}{7} \sum_{y \in \mathcal{N}_x^T} d_t^c(y). \tag{1a}$$

The second substep does the same in the \mathbb{Z} direction:

$$d''_t(x) = \frac{4}{7} d'_t(x) + \frac{3}{14} \sum_{y \in \mathcal{N}_x^Z, y \neq x} d'_t(y). \tag{1b}$$

For $x \in \partial A_t$, and $y \in A_t$, the term $d_t^c(y)$ in (1a) is replaced by $d_t^c(x)$, while the term $d'_t(y)$ in (1b) is replaced by $d'_t(x)$.

The reason for the weights in (1b) is as follows. Imagine we tessellate \mathbb{R}^3 with translates of the fundamental prism and scale the lattice $\mathbb{T} \times \mathbb{Z}$ so that the lattice points are in the centers of these prisms. The ‘‘bonds’’ in the top left frame of Fig. 2 thus all have unit length, and we eventually visualize the crystal by drawing prisms that are centered about sites of A_t . Rule (1b) ensures that diffusion on the scaled lattice is isotropic, in agreement with assumption A2.

As mentioned in the Introduction, there is also good reason to consider the more general case of diffusion with drift in the \mathbb{Z} direction, corresponding to downward (or upward) motion of the snowflake. The third diffusion substep is thus

$$d'''_t(x) = \{1 - \phi[1 - a_t(x - e_3)]d''_t(x)\} + \phi[1 - a_t(x + e_3)]d''_t(x + e_3), \tag{1c}$$

where $e_3 = (0, 0, 1)$ is the basis vector in the \mathbb{Z} direction. The parameter ϕ measures the strength of the drift, and needs to be small for the dynamics to remain diffusion limited.

2. Freezing

Assume that $x \in \partial A_t$. Let $n_t^T(x)$ be the number of its \mathbb{T} neighbors $y \in \mathcal{N}_x^T$ with $a_t^c(y) = 1$ if this number is 0, 1, or 2; we declare $n_t^T(x) = 3$ if this number equals or exceeds 3. Moreover, $n_t^Z(x) = 0$ if there are no \mathbb{Z} neighbors $y \in \mathcal{N}_x^Z$ with

$a_t^c(y) = 1$, and $n_t^Z(x) = 1$ otherwise. These two numbers represent the geometry at a boundary site x (see top right frame of Fig. 2), and determine the rate κ of freezing in this step, the rate μ of melting (step 4), and the attachment threshold β (step 3).

A proportion $1 - \kappa(n_t^T(x), n_t^Z(x))$ of the diffusive mass at x becomes boundary mass. That is,

$$b'_t(x) = b_t^c(x) + [1 - \kappa(n_t^T(x), n_t^Z(x))]d_t^c(x),$$

$$d'_t(x) = \kappa(n_t^T(x), n_t^Z(x))d_t^c(x). \tag{2}$$

The seven parameters $\kappa(i, j)$, $i \in \{0, 1\}$, $j \in \{0, 1, 2, 3\}$, $i + j > 0$ together constitute one of the ingredients of the boundary dynamics. The other ingredient μ appears in step 4 below. We assume that κ decreases in each coordinate since ‘‘more concave corners’’ at the boundary ∂A_t , i.e., those with more neighbors in A_t , should catch diffusing particles more easily.

3. Attachment

Assume again that $x \in \partial A_t$ and define the neighborhood counts as in step 2. Then x needs boundary mass at least $\beta(n_t^T(x), n_t^Z(x))$ to join the crystal:

$$\text{If } b'_t(x) \geq \beta(n_t^T(x), n_t^Z(x)), \text{ then } a'_t(x) = 1. \tag{3}$$

Again, we have seven parameters $\beta(i, j)$, $i \in \{0, 1\}$, $j \in \{0, 1, 2, 3\}$, $i + j > 0$, and the assignment makes physical sense only if β decreases in each coordinate.

In addition, we assume that $a'_t(x) = 1$ automatically whenever $n_t^T(x) \geq 4$ and $n_t^Z(x) \geq 1$. This last rule fills holes and makes the surface of the crystal smoother, without altering essential features of the dynamics.

At sites x for which $a'_t(x) = 1$, the diffusive mass becomes boundary mass: $b'_t(x) = b_t^c(x) + d_t^c(x)$, $d'_t(x) = 0$. Attachment is permanent, and there are no further dynamics at attached sites. Thus we do not model sublimation, although it may play a significant role in the last stages of snow crystal evolution (see [8], p. 27).

4. Melting

A proportion $\mu(n_t^T(x), n_t^Z(x))$ of the boundary mass at each boundary site becomes diffusive mass. Thus, for $x \in \partial A_t$,

$$b'_t(x) = [1 - \mu(n_t^T(x), n_t^Z(x))]b_t^c(x),$$

$$d'_t(x) = d_t^c(x) + \mu(n_t^T(x), n_t^Z(x))b_t^c(x). \tag{4}$$

Again, μ is decreasing in each coordinate.

III. NOTES ON COMPUTATION AND VISUALIZATION

Following the same strategy as for our previous two-dimensional model [3], the dynamics actually runs on the cubic lattice \mathbb{Z}^3 , which can be mapped onto $\mathbb{T}^2 \times \mathbb{Z}$. Our basic computational engine is written in C, but MATLAB is used for mapping and visualization. As mentioned previously, the virtual snowflakes are depicted by drawing visible boundaries of translates of the fundamental prism centered on sites of A_t .

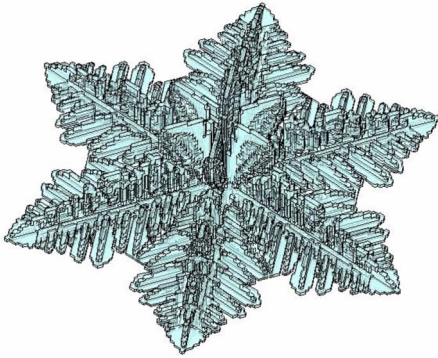


FIG. 3. (Color online) A “failed” virtual snowflake.

Since this straightforward procedure makes jagged vertical boundaries, we apply a smoothing algorithm at the boundary that enlarges the crystal by no more than one mesoscopic unit. (This algorithm has no effect on the dynamics and has not been applied to the small virtual snowflake in Fig. 2.) MATLAB’s `PATCH` routine renders the faces. For better results we then emphasize edges using the `LINE` routine.

MATLAB’s visualization tools certainly provide adequate representations for detailed investigation of the resulting crystals. They do not, however, give a satisfactory comparison with the best snowflake photographs [20,19,8], typically taken from directly above the (predominantly two-dimensional) crystal, which is in turn illuminated from below. This viewpoint can be effectively simulated by ray tracing, as implemented here by the `POV-RAY` software [27]. Our program automatically outputs a file with a triangulation of the crystal’s boundary, which is then used by the `MESH2` command in `POV-RAY`.

We would like to point out that both the algorithm and visualization procedures require considerable computing power and memory. At present, our simulations are very time consuming, barely feasible on commercial personal computers. (In fact, an adaptive resolution algorithm is necessary to make the boundary descriptions manageable.) Progress in studying virtual snowflakes is therefore quite slow, precluding systematic classification of the dynamics. Our goal has been to find representative examples that seem to replicate physical snow crystals and thereby shed light on their evolution.

When there is no drift ($\phi=0$), the initial state is a hexagonal prism, and the space is a finite lattice in the shape of hexagonal prism with appropriate periodic boundary conditions, symmetry can be exploited for computational efficiency. In fact, in this case it suffices to compute the dynamics on $1/24$ of the whole space. However, there are two good reasons for giving up complete symmetry of the rule. First, the initial state may not be symmetric, and second, the diffusion may have a drift. For computations to still proceed at a reasonable speed, we give up only reflectional symmetry around the xy plane (recall that the drift is only in the Z direction), allowing the initial state to depend on the z coordinate, but retaining its hexagonal symmetry in the x and y coordinates. This increases the space and time demands of the fully symmetric program by a factor of 2.

The program stops automatically when the density at the edge of the lattice falls below a given proportion of the initial

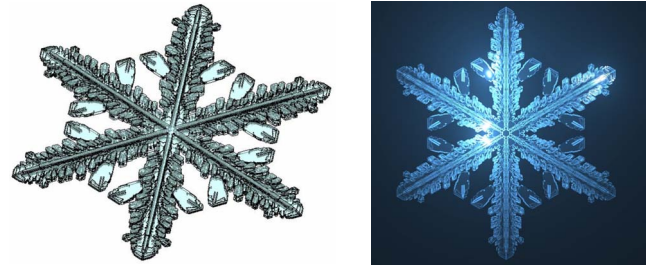


FIG. 4. (Color online) The oblique (MATLAB-rendered) and top (ray-traced) views of the crystal.

density (typically $2\rho/3$ or $\rho/2$), or when the crystal gets too close to the edge (virtual snowflake radius greater than 80% of the radius of the system).

IV. CONNECTION TO PARTIAL DIFFERENTIAL EQUATION, AND SIZE OF THE PARAMETER SPACE

For simplicity, we assume that $\phi=0$ until the last paragraph of this section. Mathematically, our algorithm is a discrete space and time version of a *free boundary* or *Stefan* problem [17,18,6]. This is a partial differential equation (PDE) in which the crystal is represented by a growing set A_t and the density (i.e., supersaturation) of vapor outside it as $u=u(x,t)$. Then u is 0 on the boundary ∂A_t , and satisfies the diffusion equation outside the crystal

$$\frac{\partial u}{\partial t} = \Delta u, \quad x \in A_t^c. \quad (5)$$

The velocity of the boundary at a point $x \in \partial A_t$ with outside normal ν is given by a function

$$w\left(\frac{\partial u}{\partial \nu}, \nu\right). \quad (6)$$

Considering the slow growth of A_t , the diffusion equation (5) may be simplified to its equilibrium counterpart $\Delta u=0$ [17,18,6], which makes this into an anisotropic version of the *Hele-Shaw* problem.

Presumably under diffusion scaling, in which space is scaled by ϵ , time by ϵ^{-2} , and $\epsilon \rightarrow 0$, the density field and the occupied set in our model converge to a solution of the Stefan problem. However, a rigorous justification for this connection at present remains elusive. Identification, or at least approximation, of the limit w for given model parameters seems more promising but is still a demanding computational task.

The boundary velocity function $w=w(\lambda, \nu) \geq 0$ is defined for $\lambda \geq 0$ and three-dimensional unit vectors $\nu \in S^2$, and specifies the boundary velocity in the direction ν when the gradient of the vapor density in that direction is λ . In order to develop a rigorous mathematical theory, the most convenient assumptions are that w is continuous in both variables, non-decreasing in λ , and satisfies $w(\lambda, \nu) \leq C\lambda$ for some constant C independent of λ and ν . Even under these conditions, one may only expect that the solution exists in a suitable generalized sense. The most promising in this context are usually

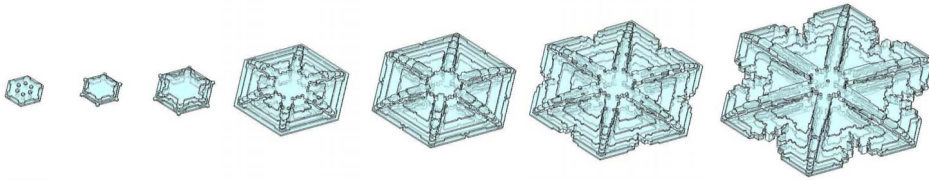


FIG. 5. (Color online) The crystal at times 820, 863, 1600, 4044, 5500, 7099, and 9500.

viscosity solutions, constructs that satisfy appropriate inequalities [28].

Under the above conditions, the nonisotropic melting version of the Stefan problem (5) and (6), which has w replaced by $-w$ in (6), has a unique viscosity solution at all times $t \geq 0$, starting from any smooth initial crystal. This is proved in [28] for the isotropic case (when w is constant); assuming the listed properties of w , the proof extends to our general setting. On the other hand, the freezing version (5) and (6) considered here presents a much greater challenge. It has long been known that the crystal's boundary will not remain smooth [29], and no general theory of existence and uniqueness of generalized solutions has been developed. The inherent difficulties will be no mystery once we present our simulations, which feature a considerable variety of singularities and instabilities. These may make direct numerical computation with the PDE questionable, explaining why numerical PDE-based models for snow-crystal growth have not been satisfactory (cf. [30]). For further mathematical theory and references, we refer the reader to [28,31].

For the sake of further discussion in this section, we posit that our scheme approximates an appropriate generalized solution, presumably of viscosity type, of (5) and (6), and thus that the macroscopic evolution of the crystal is uniquely determined by its initial state and the velocity function w .

For the model introduced in Sec. II, $w(\lambda, u)$ will be linear in λ , since the attachment and melting rates are independent of the vapor density. This may not always be the case; in fact, some of the literature even considers the possibility that w is nonmonotone in λ [18,3]. Analysis of such cases would present new theoretical challenges, and from simulations of our three-dimensional (3D) model it appears that nonmonotonicity is not needed for observed phenomena in nature. Monotone nonlinearity, arising from monotone density-dependent rates, is harder to dismiss and worth further investigation—for instance, it is possible that w vanishes for very small λ .

The function w is determined by very few physical parameters, perhaps just two: temperature and atmospheric pressure [17,18,6]. Therefore, possible evolutions from a fixed seed comprise a three-dimensional manifold (its coordinates being the supersaturation level, temperature, and pressure) in an infinite-dimensional space of possible velocities w . Much of the ongoing snow-crystal research constitutes an attempt to understand the structure of this manifold, a daunting task since the underlying (perhaps quantum) attachment physics is very poorly understood, controlled homogeneous environments are hard to design, and crystal evolution is difficult to record. Our model does not have these problems. Instead, its main weakness is the number of free parameters that need to be tuned to approximate w at a particular temperature and pressure. It helps that our parameters

have intuitive meaning, but finding a particular realistic virtual snowflake involves approximating an *a priori* infinite-dimensional object w by one of finite but high dimensionality. The challenge is compounded by very incomplete information—all that is typically observable in nature is the final crystal, which may have been subjected to numerous changes in conditions and orientation during growth, as well as sublimation and perhaps even artifacts of the recording process. It is thus no surprise that our parameter selection is an arduous and imprecise task.

Evolution of our virtual snowflakes involves tens of thousands of parallel updates of arrays comprising millions of sites, using a nonlinear local rule, and thus cannot be viewed as a tractable function of the parameters and the initial state. Our algorithm's ability to reproduce so much of the detailed structure observed in physical specimens consequently cannot be attributed to reverse engineering by twiddling a modest number of system parameters.

In the next section we will describe some *ad hoc* rules that we have used to generate our case studies, but the issue of parameter selection is in dire need of further investigation. What we can say is that the best examples are quite sensitive to perturbations in w . Thus they require good approximations and a large number of judicious parameter choices. In addition, the dependence on the initial seed is often quite dramatic. These observations underscore both the marvel and the fragility of natural snowflakes.

At the same time, we wish to emphasize the conceptual simplicity of our model. The large parameter space is a consequence of geometry rather than an excessive number of modeling ingredients. Apart from the two scalar parameters—density ρ and drift ϕ —we have only three vector parameters—attachment threshold β , freezing rate $1-\kappa$, and melting rate μ —whose high dimensionality arises from the many possible boundary arrangements. The parameter set can be reduced, but some tuning will always be necessary, as illustrated by the “random” crystal in Fig. 3. This was obtained by choosing $\kappa \equiv 0.1$, $\mu \equiv 0.001$, $\rho = 0.1$, $\phi = 0$, and all β 's equal to 1 except $\beta_{01} = 1.73$ and $\beta_{10} = \beta_{20} = 1.34$. These values are in a sensible neighborhood of the parameter space,

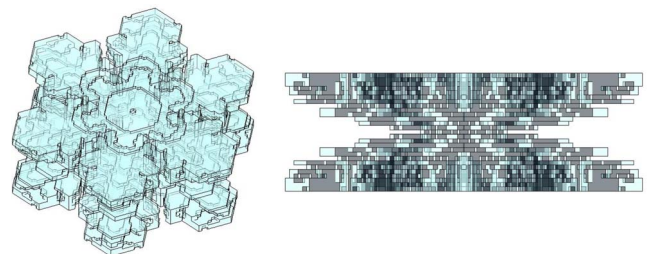


FIG. 6. (Color online) Oblique and side views of the crystal from a different initial state.

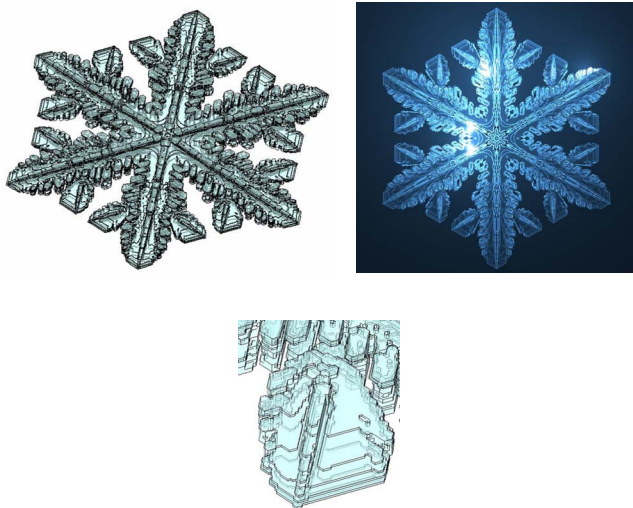


FIG. 7. (Color online) At density $\rho=0.15$, the sidebranches have particularly well-defined ridges.

but the last attachment rates were selected by chance. The result has some physically reasonable features, but one immediately notices an excessive density of branches and inordinately high ridges. In general, visual comparison with snow-crystal photographs is the only method we use to decide whether a virtual snowflake is a “failure” or a “success.”

V. EFFECTIVE CHOICE OF PARAMETERS FOR SIMULATIONS

While realistic choices of parameters require considerable guesswork, there are a few guidelines we have developed. Some come from mathematical arguments, others from experimentation; both are described in this section.

We typically choose the drift parameter ϕ last, and on the order of 0.01. This keeps $\phi \approx 1/(\text{array size})$, as required for a diffusion limit, and produces essentially one-sided markings. The rest of this section is devoted to other parameters and assumes $\phi=0$.

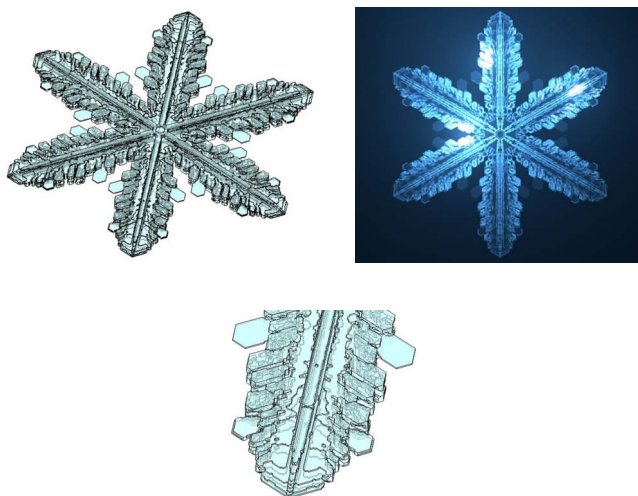


FIG. 8. (Color online) At density $\rho=0.09$, the flumes are well delineated.

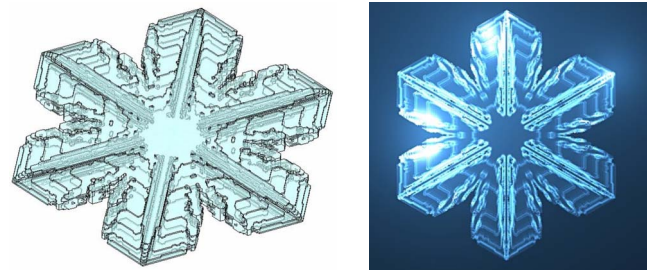


FIG. 9. (Color online) Density $\rho=0.05$ results in sectored plates.

Our simulator represents diffusion by discrete averaging in time t , which is also discrete. The bulk effects of this operation expand at rate \sqrt{t} , although the extreme radius of its influence, which is known as the *light cone* in cellular automata research, grows linearly in t . If the initial density ρ of our discrete vapor field is too large, then the crystal may expand in some direction as fast as the light cone, or perhaps fall behind it by $O(\sqrt{t})$. We call parameter sets leading to this behavior the *Packard regime*; it is clearly not physical, as it depends on the discrete nature of the averaging. However, systems of this sort are able to generate fractal plates reminiscent of Packard snowflakes [4,3] and exhibit one variety of faceting (cf. [12]). In our simulations we systematically avoid the Packard regime by keeping the density low. For the extremal points of our virtual snowflakes not to expand as fast as the light cone, the conditions are

$$(1 - \kappa_{01})\rho < \beta_{01}, \quad (1 - \kappa_{10})\rho < \beta_{10},$$

as is easy to see from the description of the rule. Our densities are typically considerably smaller, since large densities generate expansion that is too rapid to be realistic, at least in its initial stages. As mentioned previously, a surprisingly important role is also played by the choice of initial seed.

On the other hand, it is clear that a very large melting rate will stop growth altogether. This happens if the flow out of boundary mass exceeds the flow in just before that mass exceeds the threshold for attachment. A sufficient condition for continual growth in all directions is therefore

$$\mu_{01}\beta_{01} < (1 - \kappa_{01})\rho, \quad \mu_{10}\beta_{10} < (1 - \kappa_{10})\rho,$$

since the 01 and 10 boundary arrangements always have the slowest potential growth. In the great majority of examples we will present, parameters for the 20 and 10 arrangements agree. In this case, the last condition is necessary as well—if

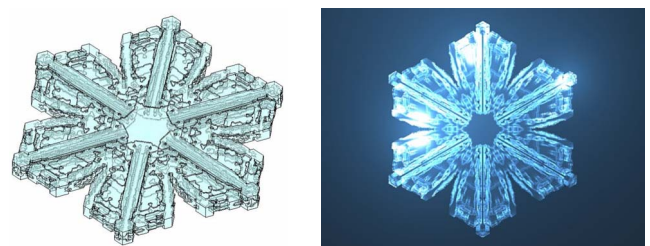


FIG. 10. (Color online) Density $\rho=0.045$ results in sectored branches.

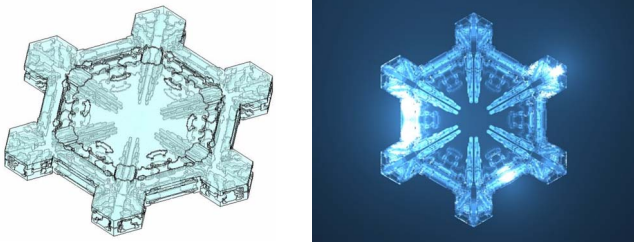


FIG. 11. (Color online) Density $\rho=0.4$ results in sandwich plates with inner ridges.

it does not hold, then the growth is convex-confined in the \mathbb{T} direction.

Let us now describe a few rules of thumb when searching for virtual snowflakes that emulate nature. We commonly start with a reduced parameter set. Namely, we set the κ 's to a common value, say, $\kappa \equiv 0.1$. Then we select two different β parameters, β_{01} and $\beta_{10} = \beta_{20} = \beta_{11}$, with all the remaining β 's fixed to 1. The size of β_{20} controls the strength of the convexifying mechanism, assumed to be the same in both the xy and z directions. Indeed, if β_{20} is large, then the crystal will remain a perfect hexagonal prism for a long time. The only other parameters are the common value of all μ 's and the vapor density ρ . This is a more manageable four-parameter space that encodes four essential elements of three-dimensional snowflake growth, each with a single tunable parameter: diffusing supersaturation level (ρ), convexifying strength (β_{20}), boundary layer smoothing (μ), and preference for the \mathbb{Z} direction over the \mathbb{T} direction (β_{01}/β_{20}). This scheme is used to identify the neighborhood of a desired morphological type in phase space. Then parameters are perturbed for added realism.

One of the most important lessons of our two-dimensional model [3] was that the melting parameter μ inhibits side-branching and is therefore important for dendrite formation. When $\mu \equiv 0$, it seems impossible to avoid an excessive density of branches. Indeed, this role of μ is easily understood. Namely, μ creates a positive density at the boundary, due to flow out of the boundary layer. This density has the effect of reducing the ambient vapor density by a fixed amount, independent of location, and hence disproportionately affects regions of smaller density. (To a very rough first approximation [6], the expansion speed is proportional to $\sqrt{\rho}/\sqrt{t}$ when $\mu \equiv 0$.) Since there is clearly less mass between branches than at the tips, growth and sidebranching there are stunted by increasing μ .

Realistic “classic” dendrites occur for a relatively narrow range of choices for μ , once the other parameters are held fixed. Typically, though, the other parameters need to be perturbed along with μ ; increasing μ alone tends to erode all complex structure.

The markings seen on snow crystal plates are sometimes called *hieroglyphs*. These often have fairly regular geometric forms, such as ridges, flumes, ribs, and circular shapes, but can also exhibit more chaotic patterns. In photomicrograph collections [14,20,19,8], it is usually unclear whether the marks are on the outside of the crystal or within what we call sandwich plates. In our experiments, the inner structures are much more prevalent, so we are glad to observe that they are abundant in nature [32]. To obtain nice outer markings, the ratio β_{01}/β_{20} needs to be sufficiently large, but there is then a tendency for the crystal to become too three dimensional. Again, the correct choice is often rather delicate. Inner markings occur generically for small values of this ratio.

Finally, different κ 's may appear to be a more natural mechanism to enforce anisotropy than different β 's, as they directly correspond to sticking, or *killing*, of particles at the crystal's boundary. However, for this effect to be substantial, the killing at the boundary must be slow and thus the κ 's need to be very close to 1; this causes the already slow growth to proceed at an even more sluggish pace. While less physically appealing, we view the β 's as a reasonable compromise for the sake of computational efficiency.

VI. VARIANTS AND EXTENSIONS OF THE MODEL

A. Uniform virtual snowflakes

Since attachment thresholds β vary, the mass of the final crystal is not uniform. There is a variant of our algorithm that removes this defect with little change in observed morphology. Assume that there is no automatic filling of holes; instead, boundary mass exactly 1 is needed for attachment when $n_t^{\mathbb{T}}(x) \geq 4$ and $n_t^{\mathbb{Z}}(x) \geq 1$. Then a uniform crystal is obtained by performing the following additional step just after step 3 in the simulator:

1. Postattachment mass redistribution

To redistribute any excess mass from the attached site to its unattached neighbors, let

$$n_t^c(x) = |\{y \in \mathcal{N}_x: a_t^c(y) = 0\}|$$

be the number of nonattached neighbors. Then, for every x with $a_t^c(x) = 0$,

$$b_t^c(x) = b_t^c(x) + \sum_{y: a_t^c(y) = 1} \frac{b_t^c(y) - 1}{n_t^c(y)}.$$

B. Simulation without symmetry

As explained in Sec. III, at the cost of a 24-fold slowdown compared to our fully symmetric model, implementation of

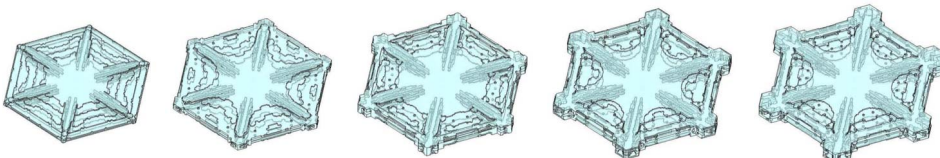


FIG. 12. (Color online) The crystal of Fig. 11 at earlier times.

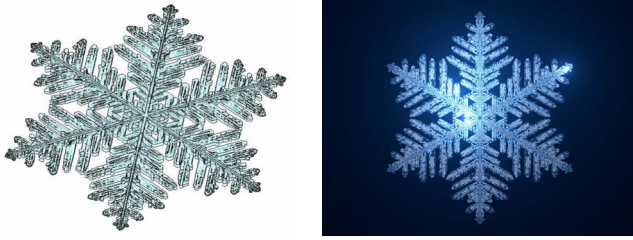


FIG. 13. (Color online) $\rho=0.105$: a fern dendrite.

the algorithm without exploiting symmetry makes it possible to study the evolution from arbitrary initial seeds. Such an extension is necessary in order to produce virtual snowflakes corresponding to exotic forms such as triangular crystals, split stars, and bullets. We have conducted a few experiments along these lines with our planar model [3], but in three dimensions a simulator dramatically faster than our current one is needed. We have future plans to develop a suitably high-performance parallel version.

C. Random dynamics

Our only three-dimensional virtual snowflakes to date are deterministic, since randomness would also require the just discussed simulation without symmetry. We propose to include an additional parameter ϵ representing residual noise on the mesoscopic scale, as we did in the two-dimensional setting [3]. Again, ϵ would need to be quite small, say on the order 10^{-5} . The random perturbation of diffusive mass from [3] is not suitable in 3D since it is not physical to violate mass conservation. Instead, a small random slowdown in the diffusion rate is more appropriate. To this end, first denote the (linear) operation on the field d_i^c in (1a)–(1c) by \mathcal{D} ; thus step 1 can be written as $d_i^{c\prime} = \mathcal{D}(d_i^c)$. Next, let $\xi_t(x)$, $t \geq 0$, $x \in \mathbb{T} \times \mathbb{Z}$, be independent random variables, equal to $\epsilon > 0$ or 0, each with probability 1/2. Here the field ξ represents the proportion of particles that refuse to diffuse at position x and time t .

The randomized step i now reads

$$d_i^{c\prime\prime} = \mathcal{D}[(1 - \xi_t)d_i^c] + \xi_t d_i^c = \mathcal{D}(d_i^c) + \xi_t d_i^c - \mathcal{D}(\xi_t d_i^c).$$

In a natural way, this represents small random temperature fluctuations in space and time.

Similarly, one could introduce a small proportion of particles that refuse to freeze in (2), or melt in (4); e.g., (2) would be replaced by

$$b_i^c(x) = b_i^c(x) + [1 - \kappa(n_i^T(x), n_i^Z(x))]d_i^c(x)[1 - \xi_t(x)],$$



FIG. 14. (Color online) $\rho=0.1$: a classic dendrite.

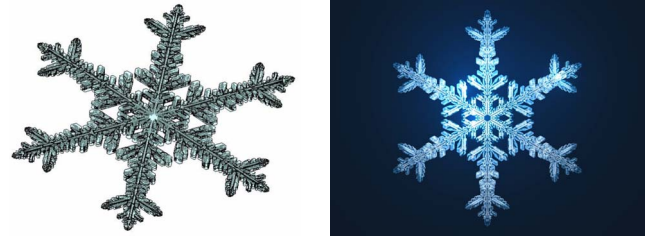


FIG. 15. (Color online) $\rho=0.095$: fewer sidebranches.

$$d_i^c(x) = \kappa(n_i^T(x), n_i^Z(x))d_i^c(x)[1 - \xi_t(x)] + d_i^c(x)\xi_t(x).$$

VII. CASE STUDY 1: RIDGES AND PLATES

Our prototypical virtual snowflake has $\rho=0.1$ and the canonical initial state of radius 2 and thickness 1. Figure 4 depicts the crystal after 70 000 time steps, when its radius is about 350. Its parameters are $\beta_{01}=2.5$, $\beta_{10}=\beta_{20}=\beta_{11}=2$, $\beta_{30}=\beta_{21}=\beta_{31}=1$, $\kappa \equiv 0.1$, $\mu \equiv 0.001$, and $\phi=0$. These parameters reflect significant convexifying strength, pronounced, but weaker, preference for horizontal growth, and weak boundary effect.

We invite the reader to compare the simulated crystal with some of the photographs in [19] and especially with Fig. 1(h) in [21], a snowflake obtained at a temperature about -13°C . We think of our length unit (the width of the fundamental prism) as about $1\ \mu\text{m}$, so even the sizes of the two objects roughly match. Both objects feature extensive branching but also regularly shaped plates, or *facets*. Simultaneous emergence of realistic branches and facets within a mathematical model with a single choice of parameters is apparently unprecedented. As anticipated by Libbrecht [6,19,8], these two aspects are thus explained by diffusion-limited aggregation, anisotropic attachment, and exchange of mass at the boundary. Two opposite mechanisms compete—vapor density depletion promotes branching instabilities, and a convexifying force repairs them—but neither is able to prevail.

Perhaps the most striking features shared by the virtual snowflake in Fig. 4 and physical ones are the *ridges*, elevations in the middle of each main branch, with less pronounced counterparts on the sidebranches. We begin by illustrating how these ridges are formed and maintained. In the process we also encounter the *branching instability*, when the initial growth of a thin hexagonal plate is no longer viable and it gives rise to the six main branches.

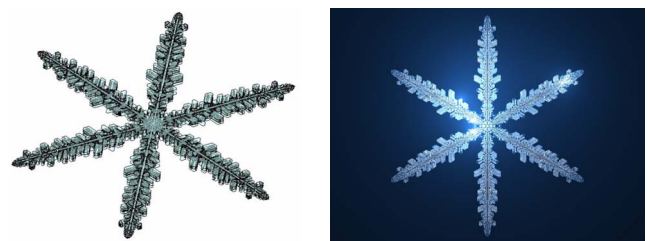


FIG. 16. (Color online) $\rho=0.09$: no significant sidebranches on this scale.

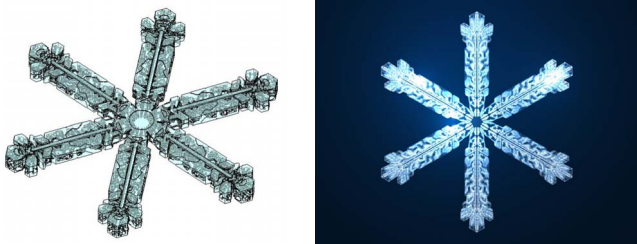


FIG. 17. (Color online) $\rho=0.082$: the tip undergoes a sandwich instability.

As shown in Fig. 5, ridges are formed quite early in the evolution, by mesoscopic bumps known as macrosteps that are near the center of the plate. This is how the ridges grow (very slowly) in the vertical direction—compare with times 4044 and 7099, which also feature such bumps. The ridges spread to a characteristic width, but sharpen to a point near the branch tip. One can also observe the commonly observed *flumes* (called *grooves* in [8]) that form on both sides of a ridge.

The small indentation that emerges, due to lower vapor density, in the middle of each prism facet at time 5500, has appeared several times before. However, this is the first instance when the growth is unable to repair it. Instead, the growth there virtually stops, while the six main arms continue to grow and eventually produce two types of side-branches: common, relatively thick double-plated branches that we call *sandwich plates*, and more unusual thin plates with their own ridges. The tip of each arm assumes its characteristic shape by the final frame of Fig. 5.

It is perhaps surprising how dramatically this scenario depends on the initial (micrometer-scale) state. Keeping everything else the same, we change the initial prism to one with radius 2 and thickness 3. The previous rather complex and aesthetically pleasing evolution is replaced by a growing double plate (Fig. 6). (Remarkably, even adding a small drift does not help matters much.) This dichotomy arises frequently in our model—within a neighborhood of the parameter space that produces planar crystals there are two stable attractors: one with outside ridges and the other a split plate with ridges on the inside. As much of the literature points out, split plates are extremely common in physical crystals (cf. [22]).

Finally, let us experiment with changing the density ρ . We exhibit five crystals (Figs. 7–11), each with the canonical initial condition and all other parameters of the prototype unchanged, but at different densities and different final times. Dramatically lower density does promote faceting [8,20], but a moderate perturbation seems to mainly promote slower growth, without a change in morphology.

The example in Fig. 11 (pictured at time 120 000) never undergoes the branching instability illustrated in Fig. 5, al-

though it does develop fairly standard ridges that persist until about time 40 000. This is the time shown in the first frame of Fig. 12; subsequent frames show the evolution in time increments of 10 000. We observe that a completely different *sandwich instability* takes place: first the tips and then the sides of the virtual snowflake thicken and develop sandwich plates. It is also clear from the time sequence that this morphological change is accompanied by a significant slowdown in growth. We should emphasize that this slowdown is not due to the depletion of mass on a finite system: much larger systems give rise to the same sandwich instability well before the edge density diminishes significantly. Neither is this slowdown accompanied by a significant growth in the Z direction—in the period depicted, the radius in the Z direction increases from 6 to 7, whereas the radius in the T direction increases from 67 to 87. Instead, much of the growth fills space between the ridges, the remnants of which end up almost completely below the surface.

Note that the virtual snowflake of Fig. 10 is also experiencing the sandwich instability at about the capture time. The difference in that case is that the growing crystal also experienced the branching instability earlier in its development.

VIII. CASE STUDY 2: CLASSIC DENDRITES

For this series of virtual snowflakes, $\beta_{01}=1.6$, $\beta_{10}=\beta_{20}=1.5$, $\beta_{11}=1.4$, $\beta_{30}=\beta_{21}=\beta_{31}=1$, $\kappa\equiv 0.1$, all $\mu\equiv 0.008$, $\phi=0$, and growth starts from the canonical initial state. The parameters reflect a very small preference for horizontal growth, a weak convexifying tendency, but a pronounced boundary layer. We will again look at how morphology is affected by different vapor densities ρ . The simulations argue persuasively that the frequency of sidebranches decreases with decreasing ρ . When $\rho=0.105$ (Fig. 13), the branches are so dense that the crystal is rightly called a fern, while the examples with $\rho=0.1$ (Fig. 14) and 0.095 (Fig. 15) have the classic look of winter iconography. These are our largest crystals, with radii around 400. A more substantial decrease in ρ eliminates any significant sidebranching on this scale, resulting in a simple star for $\rho=0.09$ (Fig. 16). As should be expected from Sec. VII, further decrease finally produces a sandwich instability at the tips, resulting in thick double plates (Fig. 17). In this instance, slow growth at the branch tips is accompanied by significant fattening in the Z direction.

The crystal in Fig. 17 is captured at about time 60 000. The series of close-ups in Fig. 18 provides another illustration of the sandwich instability—snapshots of the same virtual snowflake are shown at time intervals of 1000, starting from time 37 000. Our final example, with $\rho=0.081$ (Fig. 19), demonstrates that a further decrease in density makes the crystal increasingly three dimensional.

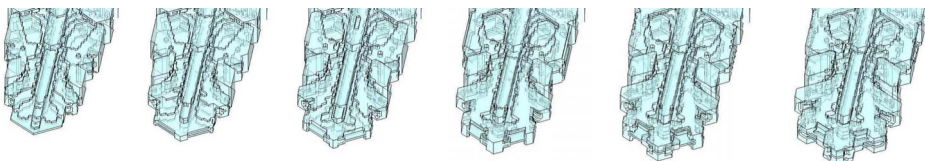


FIG. 18. (Color online) Close-up of the sandwich instability at $\rho=0.082$.

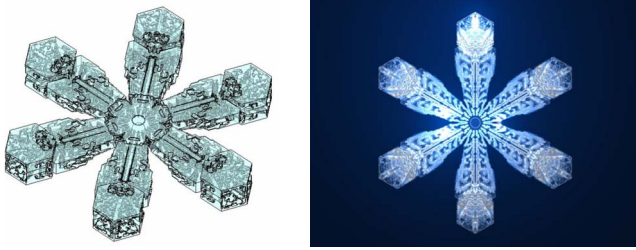


FIG. 19. (Color online) Fattening from the tip inward at $\rho = 0.081$.

IX. CASE STUDY 3: SANDWICH PLATES

When growth in the Z direction is much slower than in the xy plane, outer ridges never develop. Instead, the dynamics grows a featureless prism, which, when sufficiently thick, undergoes a sandwich instability, producing inner ridges. Much later the crystal experiences the branching instability, with platelike branches that bear a superficial resemblance to Packard snowflakes [4,2] during early stages.

Throughout the evolution the external surface of the crystal has few markings, whereas inside features include ridges and *ribs*, which signify gradual thinning of the plates from the center outward before the branching instability. The sole surface designs are *reverse shapes*, which occur when the crystal grows in the Z direction from buds that arise close to the tips. These macrostep nuclei result in rapid growth of a single layer in the T direction until this layer outlines a nearly circular hole near the crystal's center; the hole then proceeds to shrink much more slowly.

We note that this observation provides a convincing explanation for the circular markings seen on many snow-crystal photographs [8,20]. It also suggests that ribs are predominantly inner structures. While outer ribs could occur due to instabilities or changing conditions (cf. Fig. 11), there is scant evidence of them in electron microscope photographs [32], which completely obscure inner structure. On the other hand, those photos reveal an abundance of sandwich plates, which appear as the crystal centers, at the tips of the six main arms, and as sidebranches.

We now present two examples. Both start from the canonical seed and have very strong preference for horizontal growth, quite a strong convexifying tendency, and a very faint boundary layer presence. In the first, depicted in Fig. 20, $\beta_{01}=6$, $\beta_{10}=\beta_{20}=2.5$, $\beta_{11}=2$, and the remaining β 's are 1. All κ 's are 0.1, except that $\kappa_{01}=0.5$, $\mu=0.0001$, and $\rho=0.08$. The final radius of the crystal at the capture time 100 000 is about 150. Note that the main ridge is interrupted: while initially it connects the two plates (and it has darker color in the ray-traced image as the background can be seen through it), it later splits and each plate has its own ridge. There is a suggestion of this phenomenon in real crystals (e.g., [8], p. 26).

Our second example (Figs. 21 and 22) has interrupted main ridges and a few ribs. The parameter set now has $\beta_{01}=6.5$, $\beta_{10}=\beta_{20}=2.7$, and $\rho=0.15$. The remaining values are as before, and the final sizes (this one at $t=36\ 100$) are comparable. We provide a few intermediate stages and a detail of

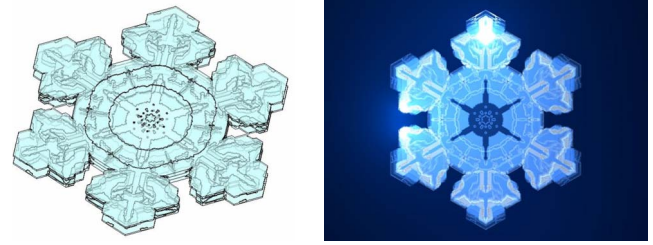


FIG. 20. (Color online) A sandwich plate.

the inner structure. Observe the buds at times 25 883 and 31 671; also note that the outermost rib at time 19 000 later disappears.

X. CASE STUDY 4: THE ROLES OF DRIFT AND MELTING

From some of the electron micrographs at [32], it appears possible that the basal facets may have ridges and other markings on one side only, while the other side is nearly featureless. As far as we are aware, no attempt has been made to “turn over” these specimens and confirm the asymmetry, but [24,25] offer a theoretical explanation. They suggest that the one-sided structure is a consequence of early growth and that ridges are actually vestiges of the skeleton of hollow prisms such as Fig. 31 in Sec. XI (see Fig. 3 of [25]). In fact, it is widely held that the micrometer-scale prism from which a prototypical snowflake evolves develops slight asymmetries in the radii of its two basal facets, and that the larger facet acquires an increasing advantage from the feedback effect of diffusion-limited growth. As a result many crystals have a stunted hexagonal plate at their center. In [13] this effect is described on p. 206 and in sketch 15 of Fig. 369.

Another potential source of asymmetry in the Z direction is identified in [22], Sec. 3.5, and [21], p. 18, based on cloud tunnel experiments in the laboratory. Planar snowflakes evidently assume a preferred orientation parallel to the ground as they slowly fall, resulting in a small upward drift of the diffusion field relative to the crystal.

We emulate these aspects of asymmetric growth by means of the drift ϕ in step (1c) of our algorithm and asymmetry of the initial seed as mentioned in Sec. III. Consider first the virtual snowflake of Fig. 1 and the closely related sectorized plate in Fig. 23. The former starts from our fundamental prism and never undergoes the sandwich instability, but develops ridges on the bottom side and an almost featureless top due to the presence of $\phi=0.01$. The dynamic parameters (which reflect a strong convexifying tendency and preference for horizontal growth, but a weak boundary layer) of the sectorized plate below are identical, but growth starts from a mesoscopic prism that is 5 cells high, with radius 7 at the top and 3 at the bottom. The idea here is to mimic the situation where the upper basal plate has established an advantage over the lower basal plate early in the evolution. As is clear from the side view, in contrast to Fig. 6, growth of the lower facet stops completely due to diffusion limitation even though the small drift offers a slight advantage in the early

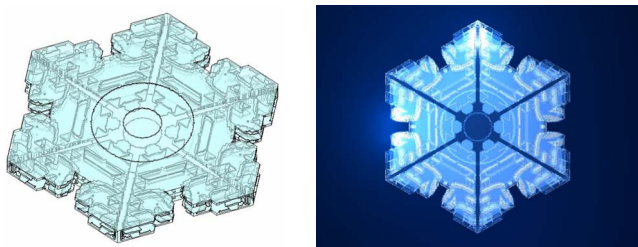


FIG. 21. (Color online) Another sandwich plate.

stages. (According to [22,23], falling snowflakes prefer the more aerodynamically stable orientation of Fig. 23.) Very many photos of physical snow crystals show evidence of such a stunted simple plate at the center; see [8], pp. 75–76, for further discussion.

The remaining examples of this section also start from slightly asymmetric seeds, experience a small drift, and have almost all their external markings on one side. Our goal is to explore the role of the melting rate, in much the same way that we studied density dependence in Sec. VII, by varying μ in a series of virtual snowflakes with all other parameters held fixed. In each instance, the seed has height 3, lower radius 2, and upper radius 1. For the next four crystals, $\beta_{01}=3$, $\beta_{10}=\beta_{20}=\beta_{11}=1.4$, $\beta_{30}=\beta_{21}=\beta_{31}=1$, $\kappa=0.1$, $\phi=0.01$, and $\rho=0.14$, so the convexifying force and the preference for horizontal growth are both moderate. Moreover, $\mu_{01}=0.002$, $\mu_{30}=\mu_{11}=\mu_{21}=\mu_{31}=0.001$ and we vary only the common value of $\mu_{10}=\mu_{20}$. This value governs the speed of tips and—as explained in Sec. V—has more effect in regions of low density, so an increase inhibits sidebranching.

Like the sectored plates just discussed, these are relatively rare virtual snowflakes with outside ridges on the main arms and most side branches. All our modeling experience suggests that crystal tips tend to symmetrize with respect to the \mathbb{T} direction, managing to avoid the sandwich instability only under quite special environmental conditions. We have seen little evidence in our simulations for the mechanism of ridge formation proposed in [24,25], so we feel that drift is a more likely explanation of one-sided structures in snowflakes.

Starting with the classic fern of Fig. 24, the common prism facet melting threshold $\mu_{10}=\mu_{20}$ is gradually increased to twice the original value in Figs. 25–27. Stellar dendrites with fewer and fewer sidebranches result, until the final virtual snowflake has only a few short sandwich plates on the sides of each arm.

The final example of this section is a classic simple star (Fig. 28), a crystal with no side branches at all and a char-

acteristic parabolic shape to its tips (cf. [8], p. 57 bottom). This elegant virtual snowflake required considerable tweaking of parameters; they are $\beta_{01}=3.1$, $\beta_{10}=1.05$, $\beta_{20}=1.03$, $\beta_{11}=1.04$, $\beta_{30}=1.02$, $\beta_{21}=1.01$, $\beta_{31}=1$, $\kappa=0.01$, $\mu_{01}=\mu_{30}=\mu_{11}=\mu_{21}=\mu_{31}=0.01$, $\mu_{10}=\mu_{20}=0.03$, $\phi=0.005$, and $\rho=0.16$. Note that convexifying is very weak, but both the preference for horizontal direction and the boundary effect are strong.

XI. CASE STUDY 5: NEEDLES AND COLUMNS

Let us now turn to the common but less familiar snow crystals that expand primarily in the \mathbb{Z} direction. As one would expect, these have β_{01} small compared to β_{10} and β_{20} , but surprisingly small advantage often suffices. We offer three virtual snowflakes that emulate their physical counterparts quite well. All start from the canonical seed. Our first example, with a substantial bias toward attachment on the basal facets, is a (simple) *needle*. In Fig. 29, $\beta_{01}=2$, $\beta_{10}=\beta_{20}=\beta_{11}=4$, $\beta_{30}=\beta_{21}=\beta_{31}=1$, $\kappa=0.1$, $\mu=0.001$, $\phi=0$, and $\rho=0.1$, so the convexifying force is very strong, but the boundary layer is weak. This virtual snowflake reproduces structure observed in nature and the laboratory: slender hollow tubes, often with cablelike protuberances at the ends (cf. [13], Fig. 135, [8], pp. 67–68).

Next, Fig. 30 simulates the common type of snow crystal known as a *hollow column*. Here the bias toward attachment on the basal facets is not as pronounced. The parameter set is $\beta_{01}=1$, $\beta_{10}=\beta_{20}=2$, $\beta_{30}=\beta_{11}=\beta_{21}=0.5$, $\beta_{31}=1$, $\kappa=0.1$, $\mu=0.01$, $\phi=0$, and $\rho=0.1$. Evidently, the hole starts developing early on. See pp. 64–66 of [8] for photos of actual hollow columns and a qualitative description of their growth.

The final example of this section is a column whose facets are hollow as well. The morphology of Fig. 31 occurs when the rates of expansion in the two directions are not very different. Photos and a description of this sort of snowflake appear on pp. 35–37 of [8]. Here $\beta_{01}=1.5$, $\beta_{10}=\beta_{20}=1.6$, $\beta_{11}=\beta_{30}=\beta_{21}=\beta_{31}=1$, $\kappa=0.1$, $\mu=0.015$, $\phi=0$, and $\rho=0.1$. The convexifying tendency is weaker; instead, the boundary effect is more pronounced.

XII. CASE STUDY 6: CHANGE OF ENVIRONMENT

In his pioneering research, Nakaya [13] reproduced several of the most striking types of snowflakes found in nature by subjecting the cold chamber in his laboratory to a precisely controlled schedule of temperature and humidity

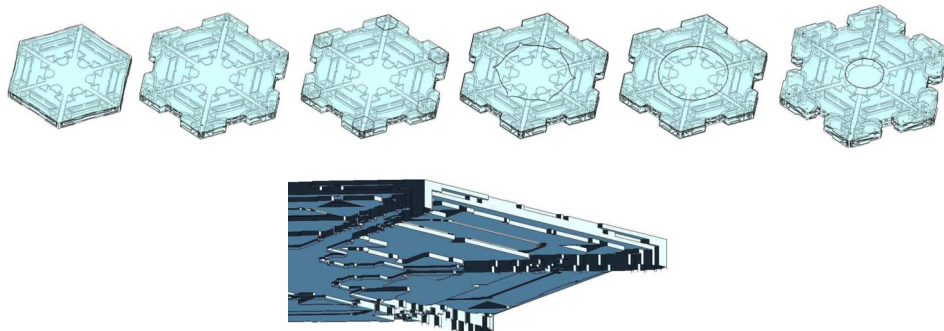


FIG. 22. (Color online) The plate of Fig. 21 at $t=19\,000$, $25\,883$, $25\,900$, $25\,950$, $26\,000$, $31\,671$. The detail is from the first time, obtained by cutting the crystal along the plane $z=0$ and zooming in on the bottom half of the upper portion.

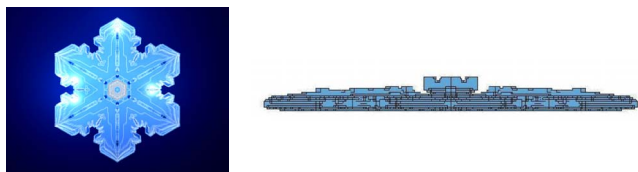


FIG. 23. (Color online) A sectored plate with a stunted double, from the top (left) and side (right).

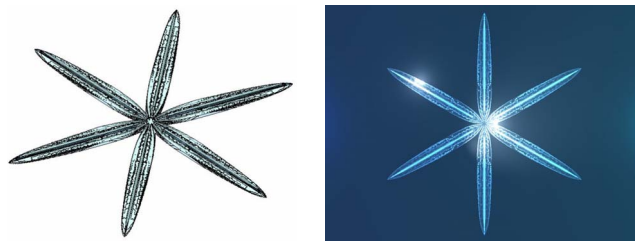


FIG. 28. (Color online) A simple star.

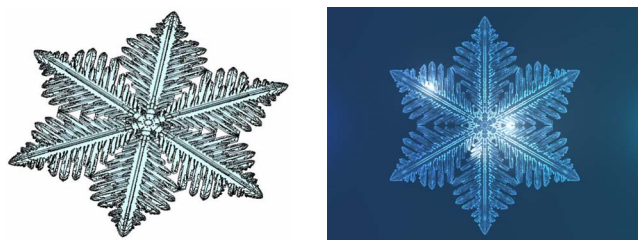


FIG. 24. (Color online) A fern dendrite for $\mu_{10}=\mu_{20}=0.005$.



FIG. 25. (Color online) Reduced sidebranching for $\mu_{10}=\mu_{20}=0.008$.



FIG. 26. (Color online) Further reduction in the number of sidebranches for $\mu_{10}=\mu_{20}=0.009$.

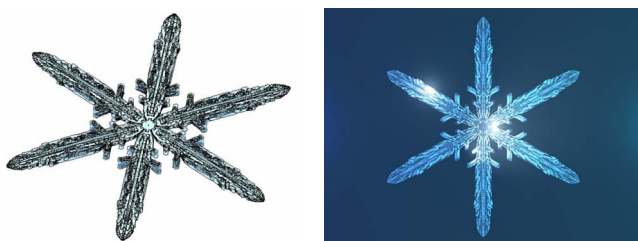


FIG. 27. (Color online) When $\mu_{10}=\mu_{20}=0.01$, very few sidebranches remain.

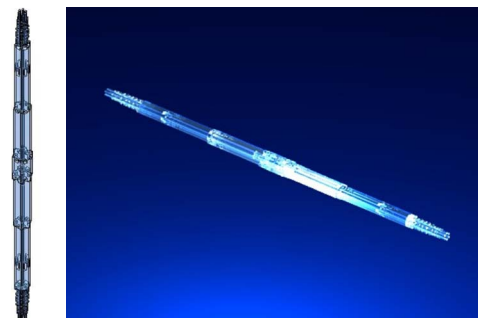


FIG. 29. (Color online) A needle.

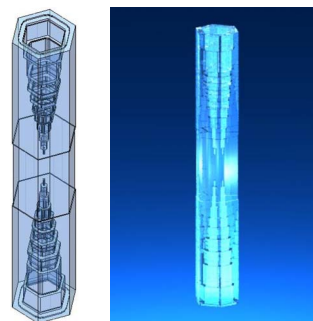


FIG. 30. (Color online) A hollow column.

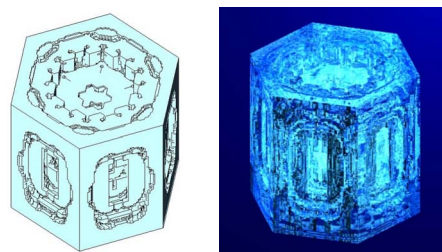


FIG. 31. (Color online) A column with hollow prism facets.

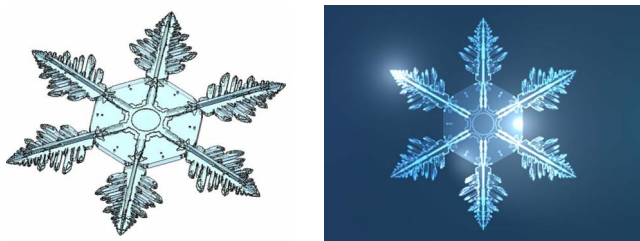


FIG. 32. (Color online) A plate with fern extensions.

changes, either sudden or gradual. Based on such experiments, he argued that *plates with dendritic extensions*, for example, are formed when a snowflake’s early growth occurs in the upper atmosphere and then it drops to another layer more conducive to branching ([13], p. 16).

In this section we mimic such varying environments by considering the effect of an abrupt change of parameters on some of our previous virtual snowflakes. Let us begin with two examples of the type cited in the last paragraph: plates with dendritic extensions. Both start from a prism that is three cells high with radius 2 at the top and 1 at the bottom. The first stage for both is a simple plate similar to the virtual snowflake of Fig. 1, but with a delayed branching instability. The initial parameters are $\beta_{01}=3.5$, $\beta_{10}=\beta_{20}=\beta_{11}=2.25$, $\beta_{30}=\beta_{21}=\beta_{31}=1$, $\kappa=0.005$, $\mu=0.001$, $\phi=0.01$, and $\rho=0.12$. The first stage runs until time 8000 in the first example, and until time 12 500 in the second. At that time most parameters remain the same, but in order to promote branching we change $\beta_{10}=\beta_{20}=\beta_{11}$ to 1.15 (1.4) and $\mu_{10}=\mu_{20}$ to 0.006 (0.004). The results, once the two virtual snowflakes have reached a radius of 200 cells, are shown in Figs. 32 and 33. Predictably, the first example has more branching in its dendritic phase since the prism facet attachment threshold is lower. The large image on the cover of [8] shows a beautiful natural example of this type.

A hybrid evolution at the opposite end of the spectrum is described in [8], pp. 51–53, and many of the most striking snowflakes in [20] are of this type. As presumably in nature, conditions need to be just right for the corresponding virtual snowflake to evolve. In this vein, we present three virtual snowflakes that begin as stellar dendrites with minimal branching and later encounter an environment promoting plates. All start from a prism of height 5 with top radius 6 and bottom radius 2. The first stage runs the simple star dynamics of Fig. 28 until time 4000, 3000, or 2000, respectively. Then new parameters for the three experiments with higher attachment thresholds are run until time, respectively, 24 000, 20 000, and close to 20 000. Common parameters



FIG. 33. (Color online) A plate with dendrite extensions.

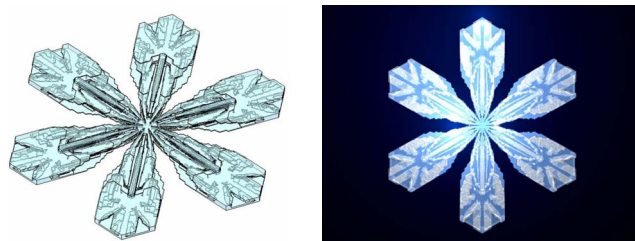


FIG. 34. (Color online) A broad-branched stellar crystal with sandwich-plate extensions.

are $\beta_{30}=\beta_{31}=1$, $\kappa=0.1$, $\rho=0.16$. In Fig. 34, the remaining parameters are $\beta_{01}=3.0$, $\beta_{10}=\beta_{20}=2.2$, $\beta_{11}=2.0$, $\beta_{21}=1.1$, $\mu=0.01$, $\phi=0.005$. Note that in this instance the branches of the star broaden considerably after the change of environment, and the tips form sandwich plates.

By raising the attachment thresholds somewhat we avoid the sandwich instability and obtain instead the sectored-plate extensions with outside ridges seen in Fig. 35. Here $\beta_{01}=3.5$, $\beta_{10}=\beta_{20}=2.45$, $\beta_{11}=2.25$, $\beta_{21}=1.1$, $\mu_{10}=\mu_{20}=0.002$, $\mu=0.001$ otherwise, $\phi=0.015$.

Our final broad-branched example interpolates between the previous two Fig. 36. The values of β are large enough to avoid the sandwich instability, but small enough that side-branching leads to sectored-plate structure of the extensions. Here $\beta_{01}=3.0$, $\beta_{10}=\beta_{20}=2.25$, $\beta_{11}=2.05$, $\beta_{21}=1.05$, $\mu=0.001$, $\phi=0.015$.

We conclude this case study with two crystals that combine a three-dimensional column and two-dimensional plates. These are the *tsuzumi*, or *capped columns*, described on pp. 69–74 of [8]. They are thought to arise when crystals are transported to higher and colder regions of the atmosphere by a passing storm. Without a preferred orientation, it is most reasonable to model these as driftless. Both our virtual snowflakes use the canonical seed and evolve with the parameters for the hollow column of Fig. 30 until time 20 000. Then they run with new parameters that promote planar growth, until time 80 000 for the first example, 60 000 for the second. Common values for the two examples are $\beta_{01}=5$, $\beta_{30}=\beta_{21}=\beta_{31}=1$, $\kappa=0.1$, $\mu=0.001$, $\phi=0$, and $\rho=0.1$. The difference is the common value $\beta_{10}=\beta_{20}=\beta_{11}$, which is 2.4 in Fig. 37 and 2.1 in Fig. 38. Higher attachment thresholds delay the branching instability in the first capped column so the caps are simple plates, as opposed to sectored plates in the second.

The transition period from column to cap in laboratory *tsuzumi* is described in some detail by Nakaya ([13], p. 221;

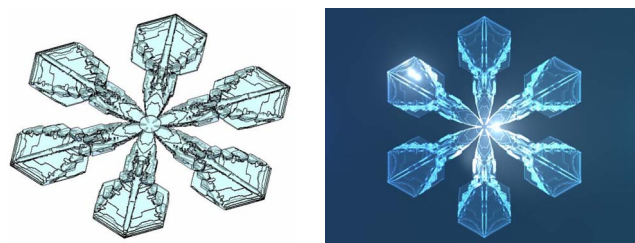


FIG. 35. (Color online) A broad-branched stellar crystal with sectored-plate extensions.

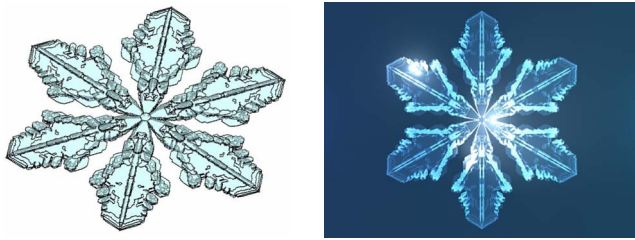


FIG. 36. (Color online) Another broad-branched stellar crystal.

see also the sketch on p. 222). We remark that our virtual snowflake versions evolve in the same way. Namely, for a considerable time after the change of environment, outward growth occurs almost exclusively along the 18 edges of the hexagonal column. This is a diffusion-limited effect similar to the hollowing in Fig. 31. Then, rather suddenly, growth in the \mathbb{T} direction takes over.

XIII. CASE STUDY 7: ECCENTRIC CRYSTALS

Our final collection features virtual snowflakes that result from a careful search through parameter space and are quite sensitive to any change. They are close to critical, near the phase boundary between dominant growth in the \mathbb{Z} and the \mathbb{T} directions. Consequently, they may be rare in nature, though variants of some of the forms have been observed, and even represent morphological types in the Magono-Lee classification [15]. All our final examples start from the canonical seed.

As mentioned in Sec. II, starting from a single cell our algorithm has a strong tendency to grow rapidly in the \mathbb{Z} direction due to the immediate onset of a *needle instability*. Even if the initial mesoscopic prism is wider in the \mathbb{T} direction, it is still quite common for this instability to arise later on if the dynamics are close to critical. After an initial phase of typical planar growth, needles suddenly nucleate at concentric locations scattered over the central plate or arms. Figure 137 of [13] shows an excellent example of this type in nature, and our first two examples illustrate a similar phenomenon in our model. The conventional explanation for such hybrid types, called *stellar crystals with needles* in [15], involves a sudden change in the environment, but this is one of several cases where our algorithm suggests that homogeneous conditions can sometimes produce the same effect.

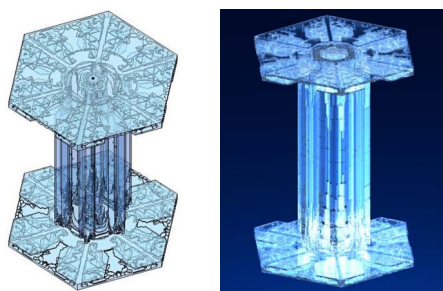


FIG. 37. (Color online) A column capped with hexagonal plates.

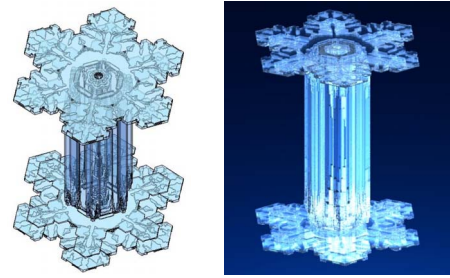


FIG. 38. (Color online) A column capped with sectorial plates.

Figure 39 has features like a classic planar snowflake that has developed *rime* from attachment of surrounding water droplets. In fact these protrusions are potential needle instabilities—the two symmetric rings close to the center and the tips are stunted needles, whereas the intermediate needles have successfully nucleated. The parameters of this virtual snowflake are $\beta_{01}=1.58$, $\beta_{10}=\beta_{20}=\beta_{11}=1.5$, $\beta_{30}=\beta_{21}=\beta_{31}=1$, $\kappa=0.1$, $\mu=0.006$, $\phi=0$, and $\rho=0.1$. Partial symmetry of bumps in many natural crystals, statistically unlikely to be the result of rime, often indicates vestiges of rims and ribs after sublimation, but can also be due to nascent needles, as in the middle specimen of Plate 116 in [13]. Since the locations where needles nucleate are quite sensitive to changes in parameters, residual randomness in the mesoscopic dynamics is apt to degrade the symmetry.

The next three examples have $\beta=1$, $\mu=0.03$, $\kappa_{10}=\kappa_{20}=0.1$, $\kappa_{30}=0.05$, and $\kappa_{11}=\kappa_{21}=\kappa_{31}=0.01$. The remaining parameters for Fig. 40 are $\kappa_{01}=0.11$ and $\rho=0.06$. This virtual snowflake is a rather extreme instance of a stellar crystal with needles in which the planar portion is a thick but very narrow simple star.

Our next two examples seem never to have been seen at all, and it is clear why: even if they managed to grow, their thin plates would be extremely brittle and susceptible to random fluctuations. They are characterized by very small differences in the growth rates. After starting as planar crystals, they suddenly nucleate thin structures extending into the third dimension. In Fig. 41 $\kappa_{01}=0.12$ and $\rho=0.057$; in Fig. 42 $\kappa_{01}=0.116$ and $\rho=0.06$. For obvious reasons, we call these *butterflakes*. They are idealizations of the *stellar crystals with spatial plates* in [15]; chaotic snow crystals with thin plates growing every which way are relatively common.

We conclude the paper with a family of five related examples. The first is a common sandwich plate (cf. [8], p. 44, lower right) with parameter values $\beta_{01}=1.41$, $\beta_{10}=\beta_{20}=1.2$,

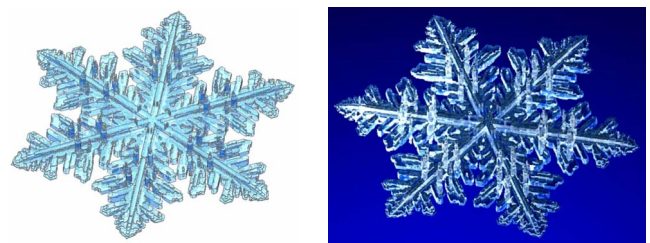


FIG. 39. (Color online) A stellar dendrite with stunted and nucleating needles.

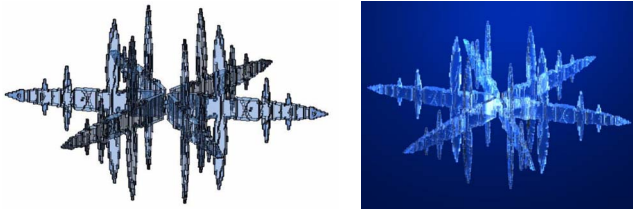


FIG. 40. (Color online) A simple star with needles.

$\beta_{11}=\beta_{30}=\beta_{21}=\beta_{31}=1$, $\kappa=0.1$, $\mu=0.025$, $\phi=0$, and $\rho=0.09$ (Fig. 43).

The remaining four are minor perturbations, which nevertheless look quite different (Figs. 44–47). Namely, even though their model parameters are constant over time, they undergo “exploding tips” quite similar to crystals such as the one in Fig. 35 that results from inhomogeneous environmental conditions. The principle behind all four variants is the same: eventually, the growing tip thickens and slows down considerably. Usually this happens close to the beginning of the evolution (as, in fact, occurred in the dynamics leading to Fig. 43), so the virtual snowflake is unremarkable. But with some experimentation we find cases when the onset of the sandwich instability is delayed and the final picture can be quite dramatic. The complex inner patterns are the result of extraordinarily intricate dynamics. Parameter values that differ from those of Fig. 43 are given in the captions.

XIV. SUMMARY AND CONCLUSIONS

We have presented a simple model of snow-crystal growth that is based on a strong convexifying force up to micrometer size and three physically reasonable mechanisms: diffusion of water molecules off the crystal, exchange between attached and unattached molecules at the boundary, and nonisotropic attachment rates that favor concave parts of the boundary over convex ones. The variety of observed phenomena we are able to replicate strongly suggests that these are the most important ingredients for the formation of physical snow crystals. Below we list further conclusions from our experiments. We are confident they hold for our mathematical model, but it remains to be seen to what extent they can be verified in the laboratory or in nature.

(a) Presence of branches and plates in snow crystals can be adequately explained by the three mechanisms built into our model.

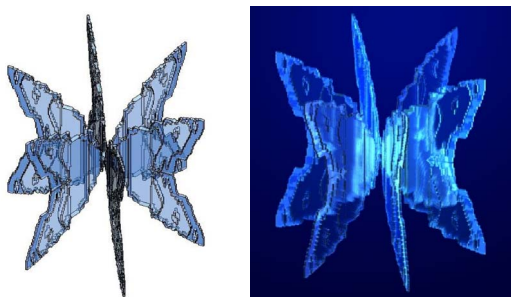


FIG. 41. (Color online) A butterflyflake with wings in the directions of the main arms.

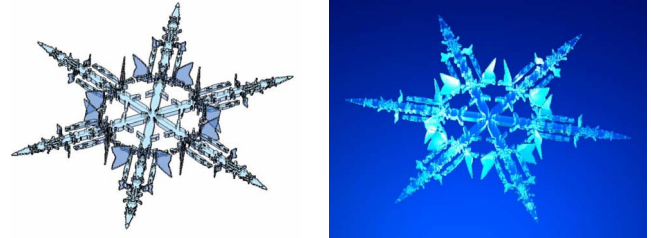


FIG. 42. (Color online) A butterflyflake with side wings.

(b) In predominantly two-dimensional crystals, the velocity of expansion in the prism direction does not need to be much larger than the one in the basal direction. In Sec. VIII, for example, this difference is less than 7%.

(c) The range of motion of a snow crystal relative to the diffusing vapor has to be quite limited during most of its growth, on the order of its final size. This motion is roughly equivalent to a small drift of water vapor, which can affect the distribution of markings on the basal facets of the crystal but otherwise has a limited effect on morphology. However, drift, along with early random fluctuations, appears to play an important role in the evolution of double plates in the case where one of them is stunted.

(d) Many, perhaps the majority of simple snow crystals are sandwich plates: two thin plates with ridges, ribs, and other markings between them. These are the result of a newly identified sandwich instability that can occur either early in the evolution, or after the crystal has reached a sizable diameter, perhaps even 100 μm or more. The latter scenario may create the illusion of a sudden change in vapor density, temperature, or pressure. The sole surface markings of sandwich plates are circular reverse shapes resulting from nucleation near the tips.

(e) Markings do appear on the surface (rather than between sandwich plates) of predominantly planar virtual snowflakes for a very narrow range of parameters, suggesting that the most attractive snow crystals occur near a phase boundary. We are nevertheless able to replicate commonly observed phenomena such as ridges, flumes, and side-branches with and without markings.

(f) Changes in environmental conditions do result in changes in morphology. These correspond well to experimental results for synthetic snow crystals [19].

(g) In dendritic crystals, lower vapor density first leads to lower frequency of sidebranches, then to sandwich instabilities and relatively thick plates.

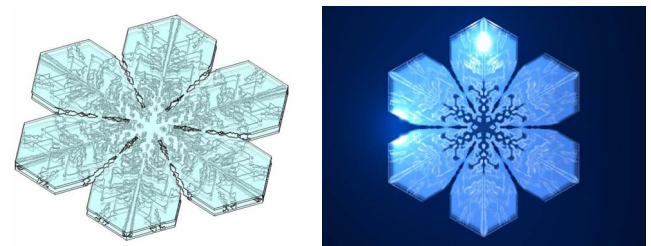


FIG. 43. (Color online) A sandwich plate with broad branches.

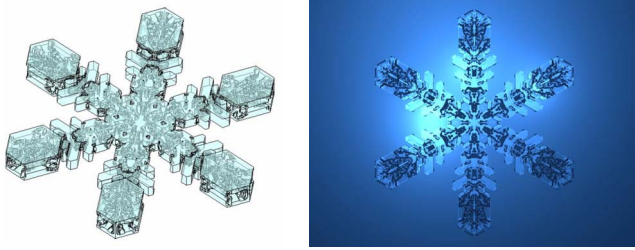


FIG. 44. (Color online) Perturbed parameters $\beta_{01}=1.25$, $\rho=0.091$.

(h) The melting rate regulates the ability of attached molecules at the boundary to detach. Increasing this rate is another mechanism to reduce sidebranching, arguably more important than reduced density.

(i) Three-dimensional structures such as needles and columns are generically hollow, and form easily when growth in the basal direction is much preferred. Prism faces of such crystals also become hollow as this preference is diminished.

(j) Very interesting phenomena occur in our virtual snowflake experiments when the preference for growth in the prism direction is only slight. These include the needle instability (nucleation of thin needles that grow in the basal direction), butterfly instability (thin plates that grow orthogonally to the main plane of growth), and exploding tips (dramatic widening of a starlike crystal's tips). Evidence for physical relevance of such eccentric dynamics is inconclusive.

As we have discussed in Sec. IV, a serious limitation of our model is poor understanding of how mesoscopic attachment rates are determined by supersaturation, temperature, and pressure. The underlying physical processes could hardly be simpler: a snow crystal arises from nothing more than the freezing of water vapor into solid ice. Yet many aspects of snow crystal growth are not understood at even a qualitative level, and for many years it was impossible to create computer models that bore even a vague resemblance to real snowflakes. The difficulty is one that always plagues bottom-up systems: processes at the molecular scale ultimately determine structure at much larger scales. In our case, dynamics at the ice surface determines the rate at which molecules condense under different conditions, and these rates in turn determine the overall structures that form. We need to understand the surface molecular dynamics in considerable detail and we need to know how crystal growth results in complex structures. The algorithm introduced here offers a

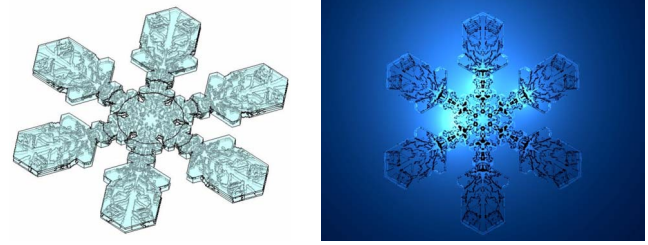


FIG. 46. (Color online) Perturbed parameter $\beta_{01}=1.19$.

viable approach to the second task, and should at least offer valuable clues for the first, thereby contributing to future understanding of the underlying physics at the molecular level.

Meanwhile, our virtual crystals seem to offer some utility in their own right. Several meteorologists are using simulation to analyze the radar and satellite microwave remote sensing properties of falling snow. This entails detailed calculation of the scattering of microwave radiation by snow crystals. One of the most significant obstacles has been the lack of a realistic and adjustable geometric model for snow-crystal shapes. To date, researchers have been forced to work entirely with two-dimensional digitized images of snow crystals collected in the field [33]. Our algorithm should expand the range of crystal habits that can be studied, enhance the available spatial resolution of those structures, and add the crucial third dimension.

Finally, the dynamics represented in our algorithm apparently govern anisotropic, diffusion-limited crystal growth in materials other than ice. For instance, freezing of the Al-Sn alloy results in crystals which are studied and modeled in [34,35]. Our approach extends easily to this case by changing the stacked triangular lattice $\mathbb{T} \times \mathbb{Z}$ to the cubic lattice \mathbb{Z}^3 . Much more intriguing are protein crystals consisting of *Neisseria gonorrhoeae* pilin, a molecule that assembles on the surfaces of bacteria and mediates the interactions of bacteria with each other and with human cells. Even though the individual molecules are very large, and have an extremely complex geometry in comparison with H_2O , Forest of the University of Wisconsin Department of Bacteriology has demonstrated [37] that aggregates may display the same mixture of hexagonal faceting and branching observed in snow crystals.

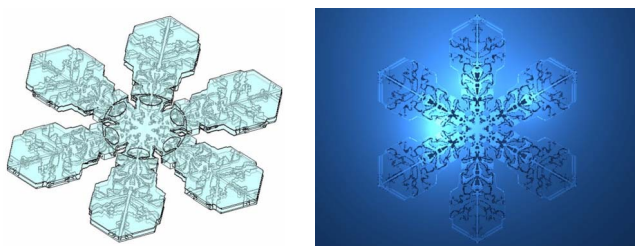


FIG. 45. (Color online) Perturbed parameter $\beta_{01}=1.5$.

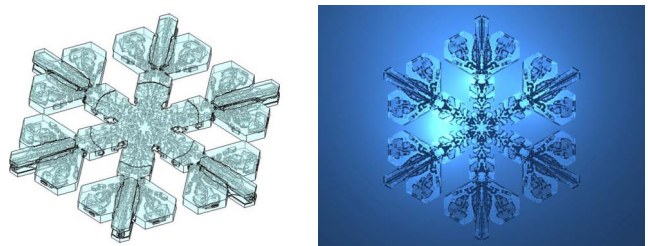


FIG. 47. (Color online) Perturbed parameter $\beta_{01}=1.25$.

ACKNOWLEDGMENTS

We thank Ken Libbrecht for sharing with us his collection of snowflake photographs and his research on snowflake physics. We also thank Antoine Clappier for introducing us

to ray tracing. J.G. was partially supported by NSF Grant No. DMS-0204376 and the Republic of Slovenia's Ministry of Science Program P1-285. D.G. was partially supported by NSF Grant No. DMS-0204018.

-
- [1] J. Gravner and D. Griffeath, *Ann. Probab.* **34**, 181 (2006).
 [2] J. Gravner and D. Griffeath, *Exp. Math.* **15**, 421 (2006).
 [3] J. Gravner and D. Griffeath, *Physica D* **237**, 385 (2008).
 [4] N. H. Packard, in *Theory and Application of Cellular Automata*, edited by S. Wolfram (World Scientific, Singapore, 1986), pp. 305–310.
 [5] C. Reiter, *Chaos, Solitons Fractals* **23**, 1111 (2005).
 [6] K. Libbrecht, *Rep. Prog. Phys.* **68**, 855 (2005).
 [7] J. T. Nelson and M. B. Baker, *J. Geophys. Res.* **101**, 7033 (1996).
 [8] K. Libbrecht, *Field Guide to Snowflakes* (Voyageur Press, St. Paul, MN 2006).
 [9] F. Frank, *Contemp. Phys.* **23**, 3 (1982).
 [10] E. Yokoyama and T. Kuroda, *Phys. Rev. A* **41**, 2038 (1990).
 [11] T. Gonda and S. Nakahara, *J. Cryst. Growth* **173**, 189 (1997).
 [12] C. Ning and C. Reiter, *Comput. Graphics* **31**, 668 (2007).
 [13] U. Nakaya, *Snow Crystals: Natural and Artificial* (Harvard University Press, Cambridge, MA, 1954).
 [14] W. A. Bentley and W. J. Humphreys, *Snow Crystals* (McGraw-Hill, New York, 1931; reprinted Dover, New York, 1962).
 [15] C. Magano and C. Lee, *J. Fac. Sci., Hokkaido Univ., Ser. 7* **2**, 321 (1966).
 [16] K. Libbrecht, *Eng. Sci.* **1**, 10 (2001).
 [17] K. Libbrecht, *J. Cryst. Growth* **247**, 530 (2003).
 [18] K. Libbrecht, *J. Cryst. Growth* **258**, 168 (2003).
 [19] K. Libbrecht, <http://www.its.caltech.edu/~atomic/snowcrystals/>
 [20] K. Libbrecht and P. Rasmussen, *The Snowflake: Winter's Secret Beauty* (Voyageur Press, Stillwater, MN 2003).
 [21] T. Takahashi, T. Endoh, G. Wakahama, and N. Fukuta, *J. Meteorol. Soc. Jpn.* **69**, 15 (1991).
 [22] K. Iwai, *J. Meteorol. Soc. Jpn.* **61**, 746 (1983).
 [23] N. Fukuta and T. Takahashi, *J. Atmos. Sci.* **56**, 1963 (1999).
 [24] J. Nelson and C. A. J. Knight, *J. Atmos. Sci.* **55**, 1452 (1998).
 [25] J. Nelson, *Cryst. Growth Des.* **5**, 1509 (2005).
 [26] Y. Furukawa and H. Nada, *J. Phys. Chem. B* **101**, 6167 (1997).
 [27] Computer code PERSISTENCE OF VISION RAYTRACER, Version 3.6, 2004, <http://www.povray.org>
 [28] I. C. Kim, *Arch. Ration. Mech. Anal.* **168**, 299 (2003).
 [29] B. Shraiman and D. Bensimon, *Phys. Rev. A* **30**, 2840 (1984).
 [30] A. Schmidt, *Acta Math. Univ. Comen.* **67**, 57 (1998).
 [31] S. Choi and I. C. Kim, *Indiana Univ. Math. J.* **55**, 525 (2006).
 [32] E. Erbe, C. Murphy, and C. Pooley, <http://emu.arsusda.gov/snows/site/default.html>
 [33] G. W. Petty and W. Huang, www.ssec.wisc.edu/meetings/jointsatmet2007/pdf/petty_snow.pdf
 [34] R. E. Napolitano and S. Liu, *Phys. Rev. B* **70**, 214103 (2004).
 [35] J. J. Hoyt, M. Asta, T. Haxhimali, A. Karma, R. E. Napolitano, R. Trivedi, B. B. Laird, and J. R. Morris, *MRS Bull.* **29**, 935 (2004).
 [36] <http://psoup.math.wisc.edu/snowflakes.htm>
 [37] K. T. Forest (private communication).